https://doi.org/10.1038/s44303-024-00060-0

Ultrahigh-field animal MRI system with advanced technological update

Yaohui Wang[1,2] ✉, Guyue Zhou[3], Haoran Chen[3], Pengfei Wu[1,2], Wenhui Yang[1,2], Feng Liu[4] & Qiuliang Wang[1,2] ✉

Animal magnetic resonance imaging (MRI) systems typically deliver superior imaging performance over conventional human MRI systems, making them a prevailing instrument in preclinical research. It is challenging to achieve the high performance of these animal MRI systems, due to the multifaceted nature of the various system components and the complexity of integration debugging. This work described the design, fabrication, measurement and integration of a 7 T animal MRI system, which exhibits several performance highlights. Both the magnet and gradient assembly adopted an ultra-shielding strategy, facilitating ease of system installation, maintenance and debugging. The main magnetic field exhibits acceptable homogeneity and stability, and the gradient coil is mechanically reliable thanks to zero-force control. The animal MRI system underwent debugging using proprietary imaging software to generate images of phantoms, fruits and organisms. Further research investigation will be performed to promote more scientific outputs with enhanced functional capabilities.

Animal magnetic resonance imaging (MRI) systems typically incorporate ultra-high-field magnets and powerful gradient assemblies, which generate very high signal-to-noise (SNR) ratios and image resolution to support fundamental research in medicine and life sciences[1–3]. To develop these ultrahigh-field animal MRI systems, the challenging aspects include but are not limited to, generating an ultrahigh magnetic field strength at the central area with acceptable field homogeneity and simultaneously shielding the strong stray field; and engineering a strong gradient magnetic field with minimal magnetic and mechanical coupling on the magnet. In contrast, generating the radio-frequency (RF) magnetic field is relatively straightforward compared to the whole-body human counterpart, due to the smaller imaging size and the lack of need for specific RF wavelength considerations[4–6]. The electrical and electronic modules include a spectrometer, gradient power supply and amplifier, and RF power supply and amplifier. The system integration and debugging depend on robust software and pulse sequences.

The research of animal MRI system has been an important topic. In superconducting magnets, apart from the inherent reliability parameters and assembly units, such as safe current margin, controllable stress level, reliable quench protection circuit[7–11], superconducting joints, switches and current leads[12,13], the most critical external parameters include a homogeneous distribution over the imaging area, 5 Gauss limit, bore size and magnet dimension. Different from permanent magnet and resistive magnet, cryogenic heat transfer is a crucial aspect of the superconducting magnet technology[14], the stable operation of the superconducting magnet needs a stable ultralow-temperature environment. After current excitation, shimming is essential to compensate for the magnetic field inhomogeneity caused by the engineering development process[15,16].

Ultrahigh gradient magnetic fields require large coil currents, which induce large Lorentz forces under an ultrahigh static magnetic field. Unbalanced Lorentz force of the gradient coils can lead to vibrations in the MRI system, posing a risk to the magnet's safety and potentially inducing magnetic field fluctuations[17,18]. In addition, shielding ultrahigh gradient magnetic fields is critical to reduce secondary magnetic field interference on the gradient magnetic field linearity[19]. Improper design of the shielded gradient coil can result in large eddy current artifacts[20]. In addition to the three-axis gradient coils, an animal gradient assembly usually includes room-temperature shim coils and passive shimming tunnels to offset magnetic field non-homogeneous harmonics in the magnetic field, as well as an efficient cooling path to dissipate the heat generated by the coils.

Animal MRI systems have been promoted by several companies for many years. In the market, Bruker animal MRI systems are currently in a

[1]Institute of Electrical Engineering, Chinese Academy of Sciences, Beijing, 100190, China. [2]School of Electronic, Electrical and Communication Engineering, University of Chinese Academy of Sciences, Beijing, 100049, China. [3]School of Electrical and Electronic Engineering, Huazhong University of Science and Technology, Wuhan, 430074, China. [4]School of Electrical Engineering and Computer Science, The University of Queensland, Brisbane, QLD, 4072, Australia. ✉e-mail: yhw@mail.iee.ac.cn; qiuliang@mail.iee.ac.cn

dominant position[21]. Some of them have been developed into hybrid instrument with other imaging modalities[22] or therapeutic devices[23]. There is also successful integration of animal MRI system using a dedicated animal superconducting magnet and human imaging platform[24]. With small gradient assembly insert, a background whole-body MRI system can be transformed into a provisional high resolution animal imaging system[25]. While these systems have significantly contributed to preclinical research and scientific studies, most works concentrated on RF coil or imaging methods improvement and the literature lacks detailed reports on the latest advanced update of the hardware performance such as superconducting magnet and gradient assembly.

This work highlights the technological advancements of a proprietary ultrahigh-field animal MRI system, mainly focusing on the superconducting magnet and gradient assembly, and the imaging evaluations were also conducted. The super-shielding and mechanical decoupling designs of the superconducting magnet and gradient assembly contribute the critical technical features of animal MRI system.

Results

Superconducting magnet

The actively-shielded 7 T animal MRI superconducting magnet coil structure is shown in Fig. 1a, which was wound by NbTi superconducting wire. The adjusting coils consist of four paratactic solenoid coils. These coils contribute magnetic field strength to the primary coils and significantly reduce the inhomogeneous harmonic components of the central magnetic field distribution, thus forming a magnetic field homogeneous region with 10 ppm homogeneity as shown in Fig. 1b. Unlike the conventional double-coil pattern, the shielding coils include an additional coil in the center. The three-coil shielding pattern creates a compact 5 Gauss line range within ±2.95 m at the axial direction and ±1.85 m at the radial direction as shown in Fig. 1c. The commercial counterpart system has a 5 Gauss range of ±3 m at the axial direction and ±2 m at the radial direction. Especially in the central section of the 5 Gauss range, the minimum radius is less than 1.4 m, which supports several safe operations such as plugging and unplugging the current lead, liquid helium infusion, cold head maintenance, etc. The coil patterns and magnetic field contours are exactly output based on the magnet design parameters displayed in Table 1, including the individual coil dimension with left axial position z_1, right axial position z_2, inner radius r_1, outer radius r_2 and corresponding current density. The critical performance parameters of the superconducting magnet design are listed in Table 2.

The superconducting shim coils design is shown in Fig. 2a, which has a layer order from inside to outside with Z2, Z1, Z3 by solenoid winding and then X, Y, ZX, ZY, X2-Y2, XY by saddle winding. We generally implemented the maximum sensitivity strategy to design the shim coils, thus it could cope with a worst inhomogeneous situation. The decoupling optimization design of shim coil Z2 makes it an alternating positive and negative seven sub-coils layout, which is much different from the conventional four-coil pattern and the mutual inductance of the magnet and shim coil is reduced from 3.9673 H to only 0.0041 H. All the coils have an identical magnetic field deviation ±1% over the central spherical area, whose magnetic field patterns are plotted in Fig. 2b. Some basic design parameters of the superconducting shim coils are listed in Table 3.

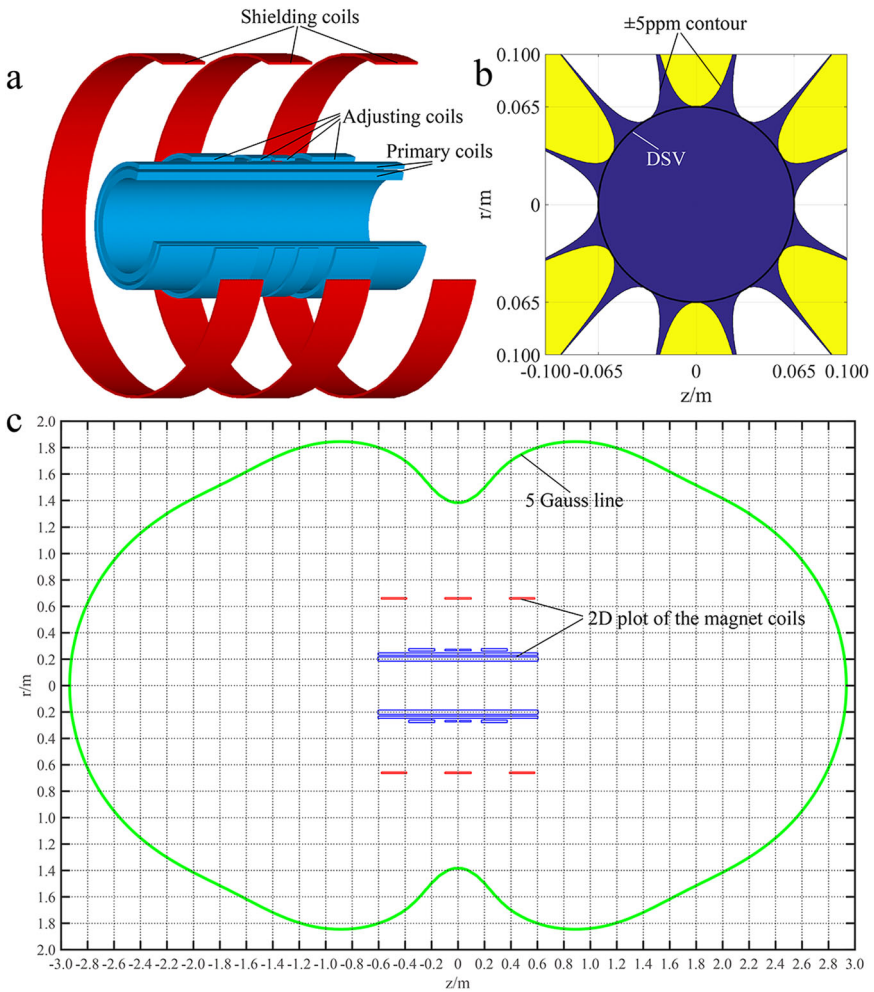

Fig. 1 | Design of a 7 T animal MRI superconducting magnet. a magnet coils, **b** central magnetic field homogeneity distribution with ±5 ppm contour and **c** 5 Gauss line range surrounding the magnet.

Table 1 | Individual coil dimension and corresponding current density

Coil dimension (m)				Current density (A/m^2)
z_1	z_2	r_1	r_2	
−0.604800	0.604800	0.185000	0.217488	7.5471781×10^7
−0.604160	0.604160	0.230200	0.247752	1.5076082×10^8
0.010253	0.098777	0.263113	0.274575	1.5031478×10^8
−0.098777	−0.010253	0.263113	0.274575	1.5031478×10^8
0.176020	0.372316	0.261139	0.279689	1.5003273×10^8
−0.372316	−0.176020	0.261139	0.279689	1.5003273×10^8
−0.099840	0.099840	0.654950	0.665582	-1.4808738×10^8
0.387918	0.579918	0.654950	0.665582	-1.4892993×10^8
−0.579918	−0.387918	0.654950	0.665582	-1.4892993×10^8

Table 2 | Design parameters of the superconducting magnet

Central magnetic field strength	7 T
Operating current	170.0320 A
DSV	130 mm
Homogeneity	10 ppm
Magnet coil dimension	Diameter: 1.33 m, Length: 1.21 m
5 Gauss range	Axial: <±2.95 m, Radial: <±1.85 m
Inductance	211.3609 H
Magnetic energy	3.5006 MJ

An illustration of the cryogenic system is shown in Fig. 3. All the superconducting coils including the magnet coils and shim coils are encapsulated in the cryogenic system in order to working at ultralow-temperature environment. The cryogenic system is consisted of a liquid helium vessel, cold shield, vacuum container and cold head. The two-stage cold head connects to the cold shield at the first stage to keep a temperature of around 50 K and suspends at the second stage into the liquid helium vessel to condense the vapored helium gas back into the liquid state. The inner wall of the vacuum container formulates the warm bore of the superconducting magnet with a diameter of 300 mm.

Gradient assembly

The gradient coils and room-temperature shim coils design is shown in Fig. 4. The gradient magnetic field strength is 200 mT/m with a magnetic field deviation ±2.5% over the homogeneous area. By minimizing the Lorentz force during the gradient coil design, the ultimate force at the designated gradient magnetic field strength within the real main magnetic field environment was controlled to be nearly zero, with a residual value of less than 0.1 N. By implementing the ultra-shielded optimization strategy, namely the stray magnetic field strength was reduced as much as possible through repeated iterations of the gradient coil design and simultaneously considered the engineering fabrication feasibility, the maximum stray field intensity for the gradient coils was minimized to 4 Gauss. This was realized with a minimum wire spacing of 3.9 mm for the X gradient coil, 4.0 mm for the Y gradient coil and 4.5 mm for the Z gradient coil. The performances of the gradient coils are listed in Table 4. For the gradient coil slew rate, it depends on the voltage, inductance and also influenced by the resistance. The equation for slew rate calculation is $S = G(U\text{-}IR)/IL$, where G is the gradient magnetic field strength, U is the voltage, I is the operating current, R is the resistance and L is the inductance. Assuming that the voltage is 500 V, by substituting the parameters in Table 4, the slew rates for the Z, X, and Y gradient coils are 503.9357 T/m/s, 1070.3454 T/m/s and 929.9312 T/m/s, respectively.

By implementing the maximizing sensitivity optimization strategy, we set the minimum wire spacing for zonal shim coils Z0, Z2, Z3, and Z4 as 3.0 mm, 3.0 mm, 3.0 mm and 3.1 mm, respectively, and 4.0 mm, 4.1 mm, 4.2 mm and 4.2 mm for the tesseral shim coils ZX, ZY, X2-Y2, XY. The transverse gradient and tesseral shim coils were manufactured using copper cutting techniques, while the axial gradient and zonal shim coils were fabricated using solenoid winding techniques. The performances of the room-temperature shim coils are detailed in Table 5.

The inner diameter of the gradient assembly is 173.4 mm. The gradient coils own high efficiency amounting to near 1 mT/m/A due to a long coil design that has copper layer amoungting to 1 m. The engraving technique on solid copper plate ensures a low resistance[26]. A dual-path cooling system supports the effective dissipation of Joule heat.

Magnet measurement and shimming

The superconducting magnet was excited to 7.02 T with magnetic field locking by a nuclear magnetic resonance (NMR) probe, as shown in Fig. 5a. After more than 7 hours of continuous sampling at a fixed position within the magnet warm bore, the decay rate of the magnetic field strength was measured to be 0.0494 ppm/h, which is stable enough for MRI application. The linear fitting calculation of the magnetic field decay rate is illustrated in Fig. 5b. Afterwards, the superconducting switches of the shim coils were individually heated to eliminate the induced currents during magnet excitation. This is necessary to evaluate the magnetic field homogeneity by removing the magnetic field interference caused by induced currents. The initial magnetic field homogeneity was then measured over a 130 mm spherical surface with a spatial positioning device, as shown in Fig. 5c, resulting in a peak-peak homogeneity of 96.32 ppm.

The magnet was shimmed firstly by superconducting shim coils and then by room-temperature iron pieces. The current input of the superconducting shim coils was calculated by a harmonic magnetic field fitting, and the corresponding currents were decomposed as 0.3978 A for Z1, −0.2359 A for X, −0.3978 A for Y, 6.0777 A for Z2, 1.3554 A for ZX, −0.3609 A for ZY, 0.1955 A for X2-Y2, −1.4538 A for XY and 0.2828 A for Z3, respectively. After the coils were excited and closed, the magnetic field homogeneity over the 130 mm spherical surface was improved to be 24.02 ppm. Subsequently, two-round passive shimming operations were conducted with separate odd and even shim trays. Two types of iron pieces were used, both having identical cross sections 24.95 mm × 24.95 mm. However, they have different thicknesses and saturation magnetization. The odd shimming operation used iron pieces with a thickness of 0.3 mm and saturation magnetization of 2.24 T. In contrast, the even shimming operation employed iron pieces with a thinner thickness of 0.05 mm and a lower saturation magnetization of 0.85 T. After passive shimming, the magnetic field homogeneity was further improved to be 7.66 ppm. The shimming results are illustrated in Fig. 6. The other homogeneity values over different imaging areas can be calculated by a harmonic decomposition method. That is 2.54 ppm over a 100 mm spherical surface, 1.57 ppm for 80 mm and 0.80 ppm for 50 mm, respectively.

MRI system integration

Due to the effective Lorentz force minimization, the force-free gradient assembly can be operated inside the magnet warm bore without any fixation. Comparatively, conventional gradient assembly has to be extended to the magnet flange and dedicatedly installed. Figure 7a shows the gradient assembly placed in the warm bore with inserted passive shim trays. The fabricated gradient assembly is shown in Fig. 7b and an in-house passively-shielded saddle RF coil[27] with inner bore diameter 80 mm is depicted in Fig. 7c. The RF transmit coil is resonated at 299 MHz with experimental measurement. The RF frontend box[28] connected to the RF coil is displayed in Fig. 7d and the integration of the spectrometer, gradient power supply and amplifier, RF power supply and amplifier is presented in Fig. 7e. The RF coil was tuned and matched when conducting the imaging operation. The

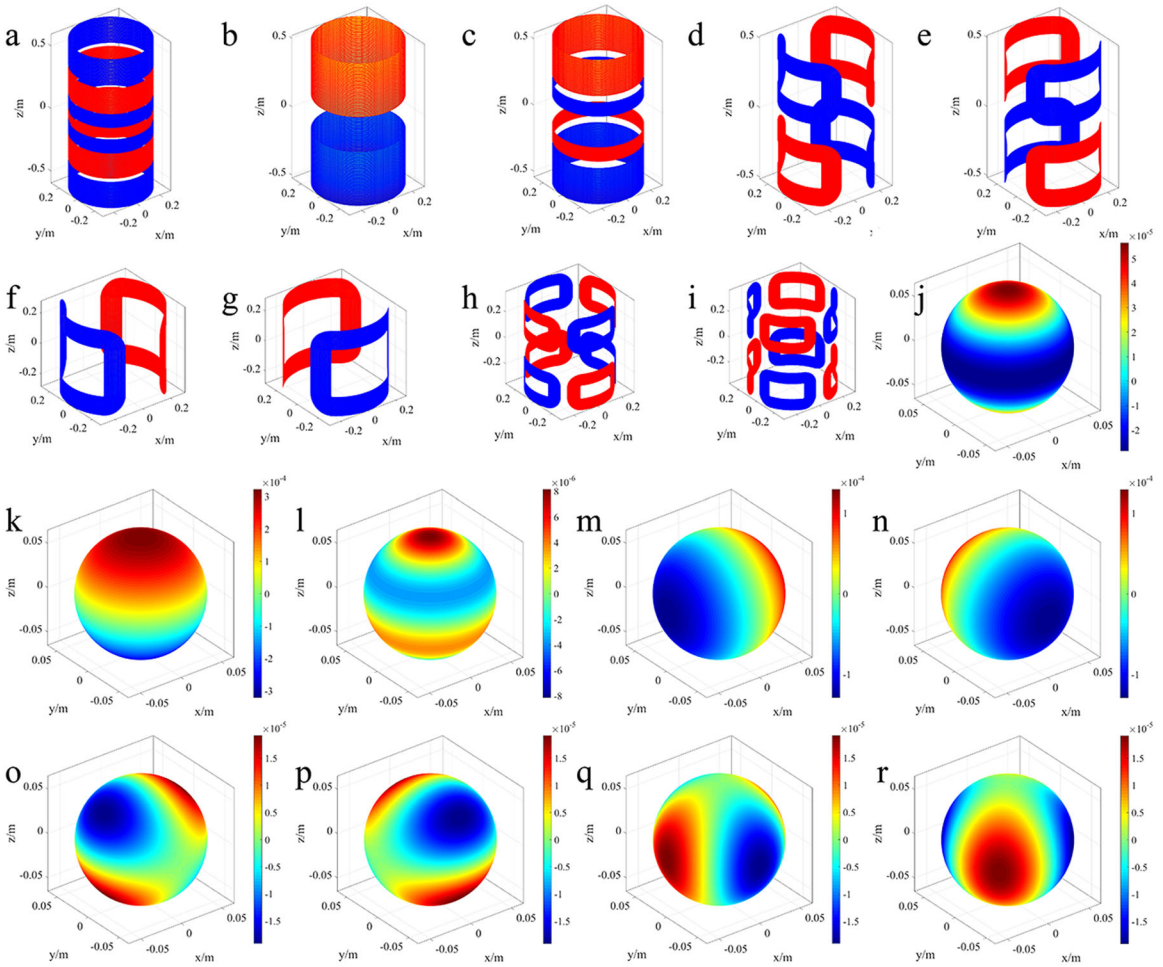

Fig. 2 | Superconducting shim coils design and corresponding magnetic field patterns. a–i shim coil of Z2 (decoupled), Z1, Z3, X, Y, ZX, ZY, X2-Y2, XY, respectively and **j–r** magnetic field patterns of corresponding shim coils.

Table 3 | Superconducting shim coil parameters

Coil type	Sensitivity	Shimming strength
Z2	0.0125 T/m^2/A	7.5446 ppm/A
Z1	0.005 T/m/A	46.4286 ppm/A
Z3	0.03 T/m^3/A	1.1770 ppm/A
X	0.002 T/m/A	18.5714 ppm/A
Y	0.002 T/m/A	18.5714 ppm/A
ZX	0.003 T/m^2/A	2.7161 ppm/A
ZY	0.003 T/m^2/A	2.7161 ppm/A
X2-Y2	0.0015 T/m^2/A	2.7161 ppm/A
XY	0.0015 T/m^2/A	2.7161 ppm/A

spectrometer has eight transceiver channels with frequency range 292 –299 MHz.

Debugging and imaging

A self-developed software package was used to debug the MRI system. The software contains routine pulse sequences, and also supports fat inhibition, water inhibition, dynamic enhanced scanning, motion artifact inhibition, diffusion imaging and angiography imaging. The initial trials of the imaging operation were based on the spin echo (SE) sequence, although there are more advanced sequences in the package. Both phantom and orange were

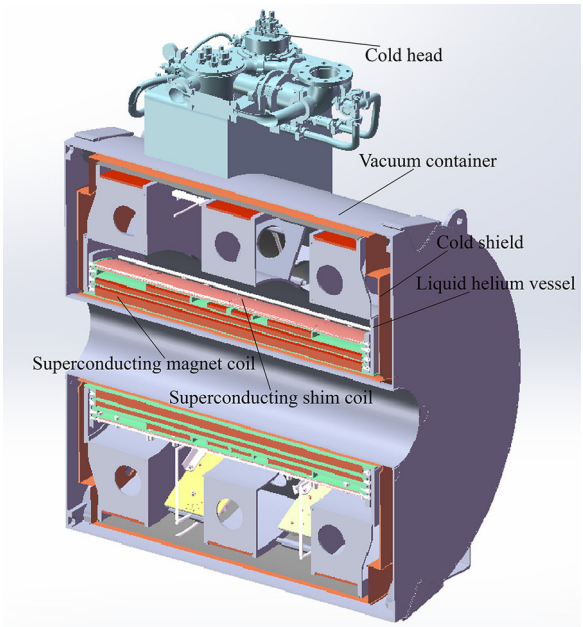

Fig. 3 | Cryogenic system of the superconducting magnet. The cryogenic system is consited of a liquid helium vessel, cold shield, vacuum container and cold head. The superconducting magnet coil and shim coil are encapsulated in the liquid helium vessel.

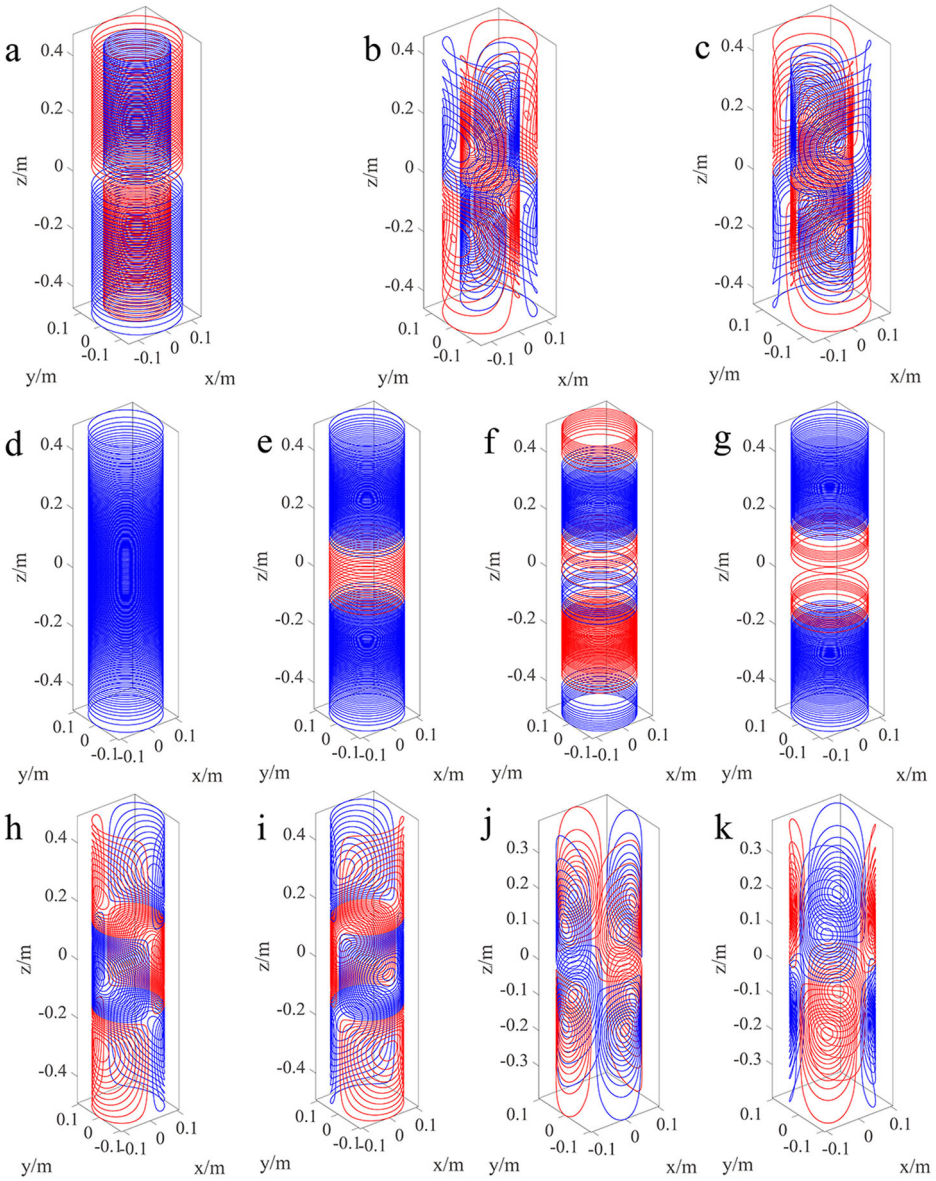

Fig. 4 | Gradient coils and room-temperature shim coils design. a–c actively-shielded Z, X and Y gradient coils, respectively, **d–g** zonal shim coils Z0, Z2, Z3 and Z4, respectively and **h–k** tesseral shim coils ZX, ZY, X2-Y2 and XY, respectively.

Table 4 | Gradient coil performances

	Z coil	X coil	Y coil
DSV	0.130 m	0.130 m	0.130 m
Gradient strength	200 mT/m	200 mT/m	200 mT/m
Field deviation	±2.5%	±2.5%	±2.5%
Operating current	201.4335 A	202.6653 A	207.2283 A
Efficiency	0.9929 mT/m/A	0.9869 mT/m/A	0.9651 mT/m/A
Loop quantity	224	120	124
Storage energy	18.4221 J	9.0828 J	10.6379 J
Power loss	7.8814 kW	4.1149 kW	4.6887 kW
Inductance	908.0402 μH	442.2754 μH	495.4379 μH
Resistance	194.2395 mΩ	100.1847 mΩ	109.1821 mΩ
Minimum wire spacing	4.5 mm	3.9 mm	4.0 mm
Fx Fy Fz	8.9651×10^{-14} N -2.0295×10^{-13} N 0.0850 N	−0.0201 N 0.0029 N -2.3978×10^{-8} N	−0.0013 N −0.0183 N 4.2055×10^{-7} N

sampled to test the instrument performance and the corresponding images are shown in Fig. 8. The diameter of the phantom is around 30 mm and the diameter of the orange is around 70 mm. The number of average is two, field of view (FOV) is around 100 mm× 100 mm, image pixel is 256 × 256, resolution is around 390 μm, and bandwidth is 25 kHz. The phantom fixed in the RF bore is shown in Fig. 8a and its images are displayed in Fig. 8b with a signal-to-noise (SNR) ratio of 167.6. Due to the limitations of RF bore size, the orange sit snugly against the inner bore where the B1 field is highly inhomogeneous and thus its edges have some dark shadows, which are shown in Fig. 8c and Fig. 8d, respectively.

The debugging processes included determining the center frequency, testing the nuclear magnetic resonance spectrum, selecting pulse sequence, setting FOV, slice thickness and sampling matrix, etc. After the debugging, a rat experiment using SE sequence with time of echo (TE) 10 ms and time of repetition (TR) 50 ms was conducted, and the diameter of the rat head is around 40 mm. The FOV is around 100 mm × 100 mm, acquisition matrix size is 256 × 256, and the slice thickness is 1 mm. To ensure safe and reliable experimental operations, the rat was anesthetized. The SE images are shown in Fig. 9. The physiological structure of the rat can be revealed from these images, and minimal artifacts and external noise interference were observed.

Table 5 | Room-temperature shim coil performances

Zonal room-temperature shim coils				
	Z0 coil	**Z2 coil**	**Z3 coil**	**Z4 coil**
DSV	0.130 m	0.130 m	0.130 m	0.130 m
Field deviation	±1%	±1%	±1%	±1%
Sensitivity	0.3833 mT/A	9.9655 mT/m^2/A	46.7054 mT/m^3/A	190.4765 mT/m^4/A
Shimming strength	54.7598 ppm/A	6.0149 ppm/A	1.8324 ppm/A	0.4857 ppm/A
Loop quantity	218	190	152	166
Inductance	2626.9 μH	1771.7 μH	999.2 μH	1498.7 μH
Resistance	3267.9 mΩ	2899.8 mΩ	2361.1 mΩ	2623.6 mΩ
Minimum wire spacing	3.0 mm	3.0 mm	3.0 mm	3.1 mm
Tesseral room-temperature shim coils				
	ZX coil	ZY coil	X2-Y2 coil	XY coil
DSV	0.130 m	0.130 m	0.130 m	0.130 m
Field deviation	±1%	±1%	±1%	±1%
Sensitivity	12.3656 mT/m^2/A	11.9262 mT/m^2/A	1.7241 mT/m^2/A	1.6692 mT/m^2/A
Shimming strength	3.7274 ppm/A	3.5950 ppm/A	3.1187 ppm/A	3.0194 ppm/A
Loop quantity	86	86	96	96
Inductance	381.3387 μH	379.9515 μH	171.2598 μH	175.1413 μH
Resistance	429.3680 mΩ	424.1629 mΩ	309.7628 mΩ	309.4713 mΩ
Minimum wire spacing	4.0 mm	4.1 mm	4.2 mm	4.2 mm

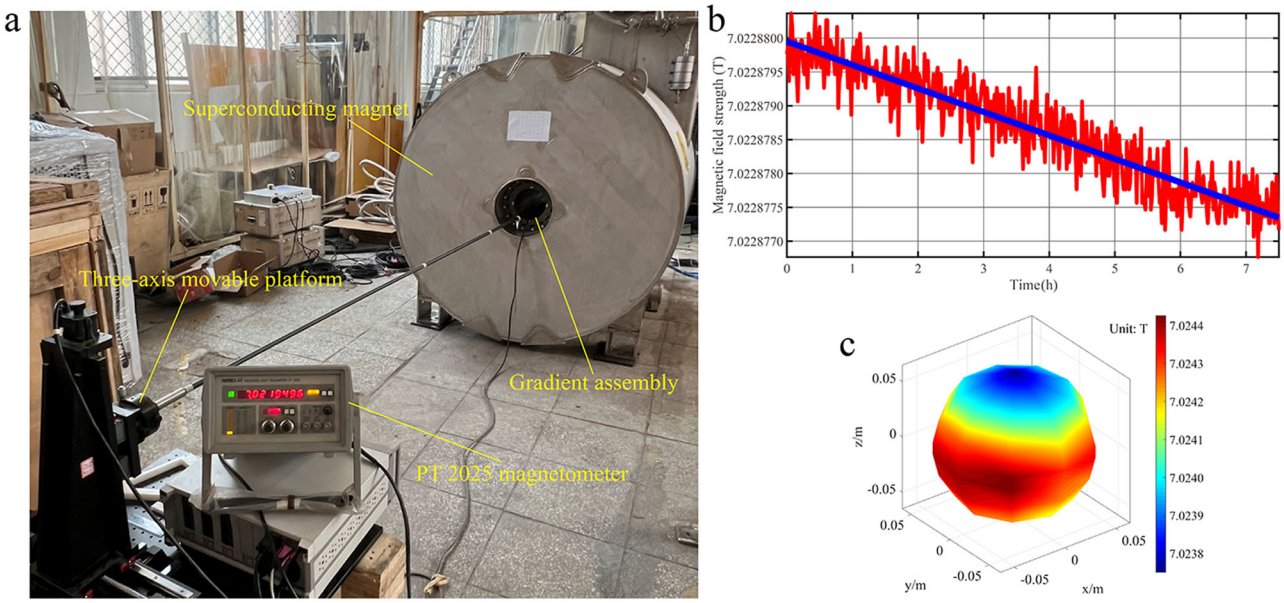

Fig. 5 | Magnetic field measurement of the fabricated superconducting magnet. a magnetic field locking by an NMR probe, **b** magnetic field decay rate evaluation and **c** magnetic field distribution over a 130 mm spherical surface.

Discussion

A 7 T animal MRI system was developed, including all the hardware components in the entire machine. During the development of critical components, some distinctive technologies were employed. The magnet has a superior shielding performance, characterized by a significantly reduced 5 Gauss line range compared to its commercial alternatives. Through the combined application of superconducting shimming and passive shimming, the ultimate magnetic field homogeneity was achieved at 7.66 ppm within a 130 mm spherical volume. The magnetic stability of the closed-loop magnet system reached 0.0494 ppm/h. These homogeneity and stability metrics are sufficient for standard MRI operations. In the design of gradient coils, a strategy to minimize the maximum stray field was implemented to ensure gradient assembly experiences non-observable eddy current interference during experimental measurements. Meanwhile, the minimization of Lorentz force resulted in residual forces less than 0.1 N at full gradient magnetic field strength, thus creating safe and convenient mechanical installation conditions for the gradient assembly.

Using our in-house developed RF coil, software, and console integration platform, we successfully acquired magnetic resonance images of phantoms, fruits and organisms. Although there are many

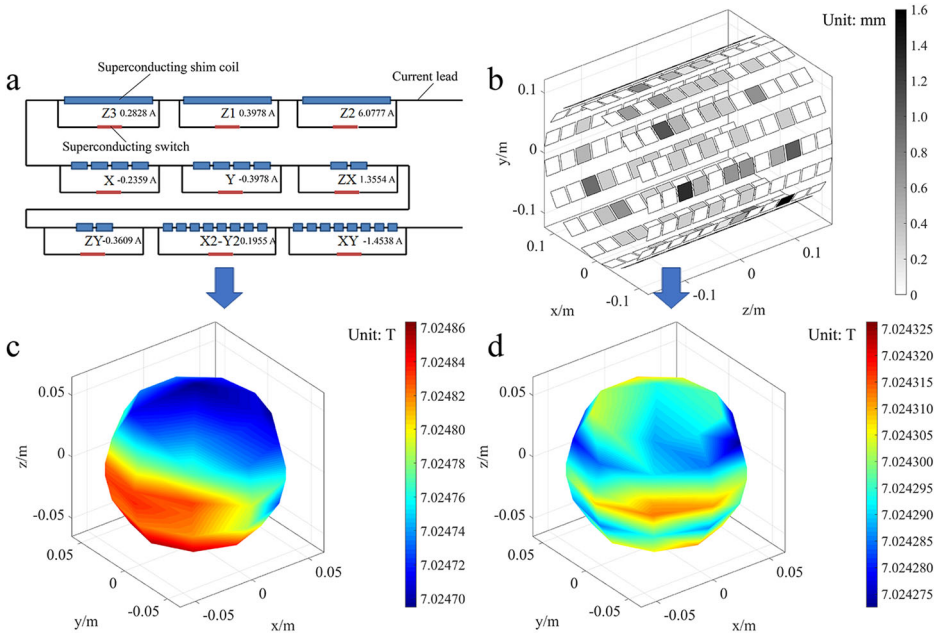

Fig. 6 | Superconducting and passive shimming results. a current input on the superconducting shim coils, **b** iron pieces distribution in the shim slots, **c** magnetic field distribution over the 130 mm spherical surface after superconducting shimming and **d** magnetic field distribution over the 130 mm spherical surface after passive shimming.

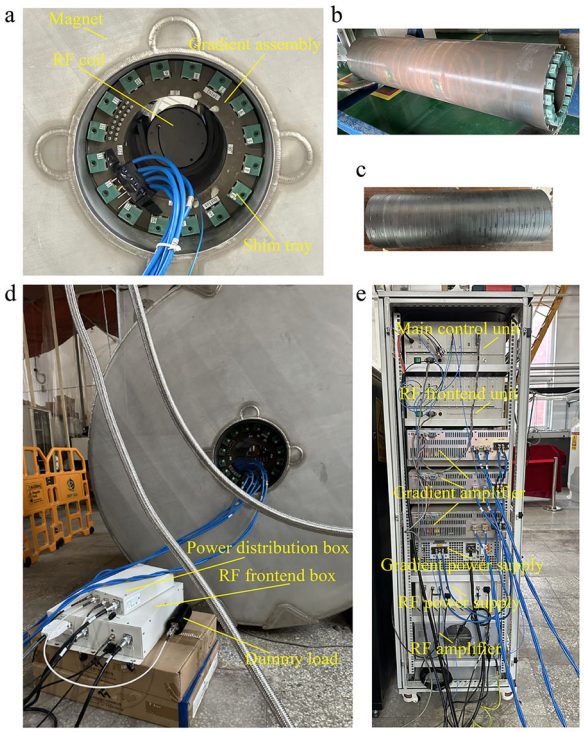

Fig. 7 | Integration of the MRI system. a Gradient assembly and RF coil in the magnet warm bore, **b** fabricated gradient assembly, **c** RF coil for testing, **d** RF frontend connection and **e** integration of the console and power system.

advanced methods to improve the imaging functions, we mostly focused on hardware development so as to providing a platform for animal model scientific research. With the advanced hardware technological update, it is feasible to develop more specialized magnetic resonance function.

Methods

A compensating field method was used to homogenize the central magnetic field distribution at a diameter of spherical volume (DSV) of 130 mm. The magnet was actively shielded, achieving a very compact range of 5 Gauss. The magnet coil structure was configured into four layers: two inner nested primary coils, an outer adjusting coil layer and an outermost shielding coil layer. An inverse electromagnetic optimization technique was applied to simultaneously achieve the magnetic field target in both the central homogeneous region and the surrounding shielding area[29].

A total of nine coils were designed, including Z, X, Y, Z2, ZX, ZY, X2-Y2, XY, and Z3. The Z2 coil was specially considered with inductance decoupling from the magnet to mitigate quench damage[30]. To minimize winding deviation, the tesseral shim coils were designed with a quasi-saddle geometry[31]. Each superconducting shim coil is connected in series, equipped with independent superconducting switches and current lead, decoupled from the magnet.

The gradient assembly was designed with a force minimization to decouple the mechanical interaction between the gradient assembly and the magnet[32]. For the mitigation of magnetic coupling between the gradient coils and the magnet, a strong shielding strategy was implemented. The shielding strategy was realized by a series of design trials, each with progressively decreasing constraints on stray field intensity. The criterion used to determine the limiting factor for stray field intensity is the minimum wire spacing. This ensures the feasibility of fabricating the coil without local filamentary wires that could potentially result in a burning point. In this work, we considered the minimum wire spacing for the gradient coils to be approximately 4 mm. With this criterion, we finally found the minimum stray field strength constraint for the gradient coil design. To determine the sensitivities of room-temperature shim coils, we tried to achieve the highest possible number of turns until reaching the minimum wire spacing of around 3 mm for zonal coils and 4 mm for tesseral coils.

The RF coil is a shielded saddle coil that resonates at around 7 T, and the software is a self-developed one with routine pulse sequences. The console, power supply and amplifiers were commercially acquired and self-assembled. All these components were integrated into a complete animal MRI system.

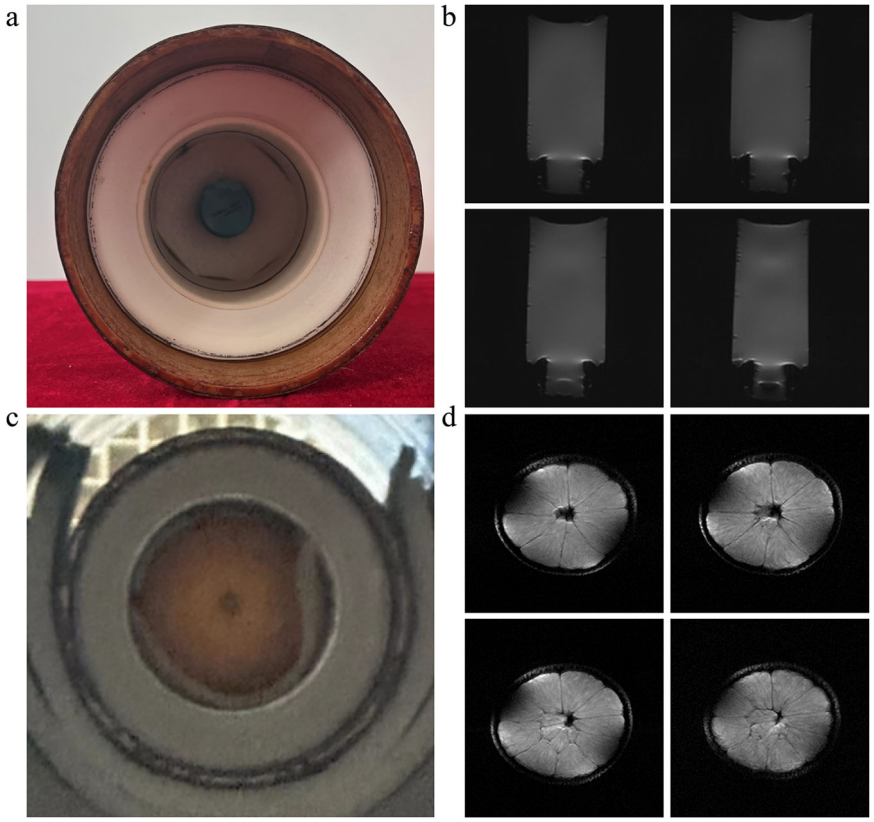

Fig. 8 | Experimental test of the instrument performance. a a phantom in the RF coil, **b** phantom image, **c** an orange in the RF coil and **d** orange image.

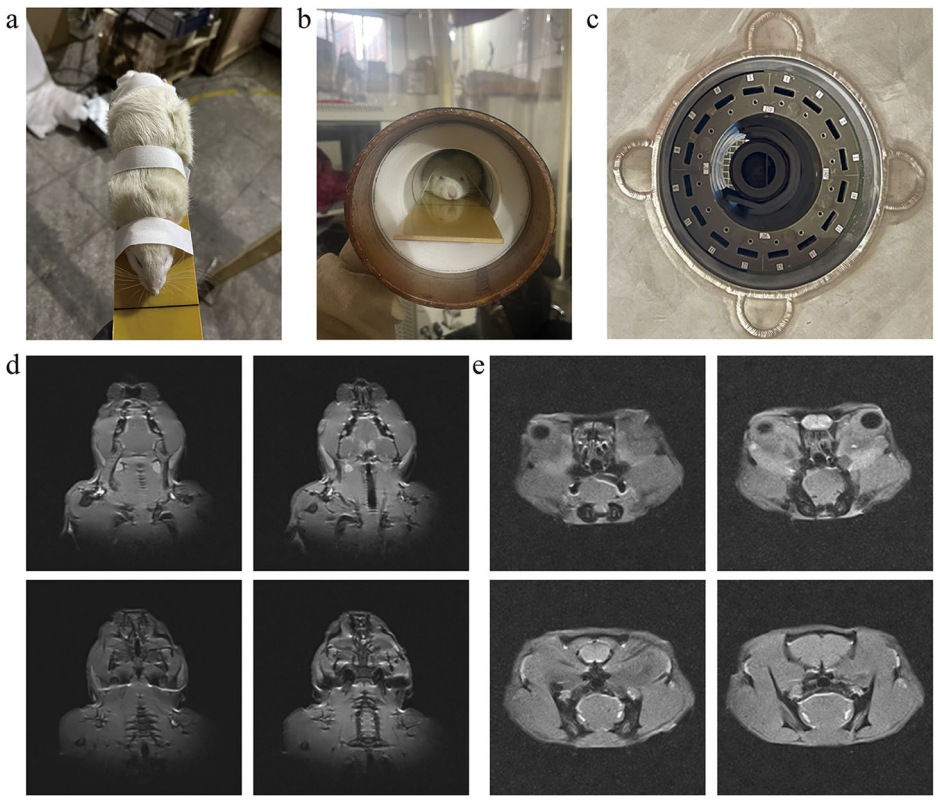

Fig. 9 | Biological experiment on the MRI system. a an anesthetized rat fixation on a plate, **b** a rat in the RF coil, **c** inserting the RF coil into the bore of the gradient assembly and (**d**, **e**) rat images from different slices and orientations.

Data availability

No datasets were generated or analysed during the current study.

Code availability

There is no original code in this work.

Received: 22 June 2024; Accepted: 19 November 2024;
Published online: 11 December 2024

References

1. Benveniste, H. & Blackband, S. MR microscopy and high resolution small animal MRI: applications in neuroscience research. *Prog. Neurobiol.* **67**, 393–420 (2002).
2. Hoyer, C., Gass, N., Weber-Fahr, W. & Sartorius, A. Advantages and challenges of small animal magnetic resonance imaging as a Translational Tool,. *Neuropsychobiology* **69**, 187–201 (2014).
3. Kim, S.-G. & Ugurbil, K. High-resolution functional magnetic resonance imaging of the animal brain. *Methods* **30**, 28–41 (2003).
4. Regatte, R. R. & Schweitzer, M. E. Ultra-high-field MRI of the musculoskeletal system at 7.0T. *J. Magn. Reson. Imaging* **25**, 262–269 (2007).
5. Ladd, M. E. et al. Pros and cons of ultra-high-field MRI/MRS for human application. *Prog. Nucl. Magn. Reson. Spectrosc.* **109**, 1–50 (2018).
6. Williams, S. N., McElhinney, P. & Gunamony, S. Ultra-high field MRI: parallel-transmit arrays and RF pulse design. *Phys. Med. Biol.* **68**, 02TR02 (2023).
7. Wang, Y. et al. Actively-shielded superconducting magnet design of a large-Bore 7 T animal MRI scanner. *IEEE Trans. Appl. Superconductivity* **30**, 1–4 (2020).
8. Chen, J. & Jiang, X. Stress analysis of a 7 T actively shielded superconducting magnet for animal MRI. *IEEE Trans. Appl. Superconductivity* **22**, 4903104 (2012).
9. Wang, Y. et al. Design, fabrication and measurement of a 3 T cryogen-free animal MRI superconducting magnet. *IEEE Trans. Appl. Superconductivity* **34**, 1–4 (2024).
10. Chen, J. & Jiang, X. Protection circuit and quench simulation of a 7 T superconducting magnet for animal MRI. *IEEE Trans. Appl. Superconductivity* **23**, 4701104 (2013).
11. Li, Y. et al. A passive quench protection design for the 9.4 T MRI superconducting magnet. *IEEE Trans. Appl. Superconductivity* **24**, 1–5 (2014).
12. Liu, S., Jiang, X., Chai, G. & Chen, J. Superconducting joint and persistent current switch for a 7-T animal MRI magnet. *IEEE Trans. Appl. Superconductivity* **23**, 4400504 (2013).
13. Manso Jimeno, M., Vaughan, J. T. & Geethanath, S. Superconducting magnet designs and MRI accessibility: A review. *NMR Biomedicine* **36**, e4921 (2023).
14. Bredy, P. et al. Cryogenics around the 11.7 T MRI Iseult magnet. *IEEE Trans. Appl. Superconductivity* **20**, 2066–2069 (2010).
15. Haskell, M. W., Nielsen, J.-F. & Noll, D. C. Off-resonance artifact correction for MRI: A review. *NMR Biomedicine* **36**, e4867 (2023).
16. Gach, H. M., Curcuru, A. N., Mutic, S. & Kim, T. B0 field homogeneity recommendations, specifications, and measurement units for MRI in radiation therapy. *Med. Phys.* **47**, 4101–4114 (2020).
17. Sakhr, J. & Chronik, B. A. Vibrational response of a MRI gradient coil cylinder to time-harmonic Lorentz-force excitations: An exact linear elastodynamic model for shielded longitudinal gradient coils. *Appl. Math. Model.* **74**, 350–372 (2019).
18. Hiltunen, J. et al. Quantification of mechanical vibration during diffusion tensor imaging at 3 T. *NeuroImage* **32**, 93–103 (2006).
19. Wang, Y. et al. Gradient coil design with enhanced shielding constraint for a cryogen-free superconducting MRI system. *Magn. Reson. Lett.* **4**, 100086 (2024).
20. Graham, M. S., Drobnjak, I. & Zhang, H. Realistic simulation of artefacts in diffusion MRI for validating post-processing correction techniques. *NeuroImage* **125**, 1079–1094 (2016).
21. Waterton, J. et al. Repeatability and reproducibility of longitudinal relaxation rate in 12 small-animal MRI systems. *Magn. Reson. Imaging* **59**, 121–129 (2019).
22. Thiessen, J. D. et al. MR-compatibility of a high-resolution small animal PET insert operating inside a 7 T MRI. *Phys. Med. Biol.* **61**, 7934 (2016).
23. Zhang, X. et al. Evaluation of a developed MRI-guided focused ultrasound system in 7 T small animal MRI and proof-of-concept in a prostate cancer Xenograft model to improve radiation therapy. *Cells* **12**, 1–21 (2023).
24. Felder, J., Celik, A. A., Choi, C.-H., Schwan, S. & Shah, N. J. 9.4 T small animal MRI using clinical components for direct translational studies. *J. Transl. Med.* **15**, 264 (2017).
25. Herrmann, K. et al. Possibilities and limitations for high resolution small animal MRI on a clinical whole-body 3T scanner. *Magn. Reson. Mater. Phys., Biol. Med.* **25**, 233–244 (2012).
26. Handler, W. et al. Design and construction of a gradient coil for high resolution marmoset imaging. *Biomed. Phys. Eng. Express* **6**, 045022 (2020).
27. Parsa, J. & Mohammadzadeh, M. Design and fabrication of a new multi-loop saddle coil for 1.5 T MRI. *Rev. Sci. Instrum.* **90**, 114707 (2019).
28. Vaughan, J. T., Haupt, D. N., Noa, P. J., Vaughn, J. M. & Pohost, G. M. RF front end for a 4.1 Tesla clinical NMR spectrometer. *IEEE Trans. Nucl. Sci.* **42**, 1333–1337 (1995).
29. Wang, Y. et al. Actively-shielded ultrahigh field MRI/NMR superconducting magnet design. *Superconductor Sci. Technol.* **35**, 014001 (2022).
30. Zhu, X. et al. The design of decoupled even-order zonal superconducting shim coils for a 9.4 T whole-body MRI. *IEEE Trans. Appl. Superconductivity* **26**, 1–8 (2016).
31. Wang, Y., Wang, Q., Qu, H., Liu, Y. & Liu, F. Tesseral superconducting shim coil design with quasi-saddle geometry for use in high-field magnet system. *Rev. Sci. Instrum.* **90**, 094705 (2019).
32. Wang, Y. et al. A dichotomization winding scheme on a novel asymmetric head gradient coil design with an improved force and torque balance,. *IEEE Trans. Biomed. Eng.* **66**, 3339–3345 (2019).

Acknowledgements

This work is supported by the National Natural Science Foundation of China (Grant No. 52293423 and Grant No.52277031) and the International Partnership Program of Chinese Academy of Sciences (Grant No. 182111KYSB20210014).

Author contributions

Y. Wang: magnet coil and gradient assembly design, measurement, shimming, system integration, manuscript writing. G. Zhou, H. Chen and P. Wu: shimming, debugging. W. Yang: imaging software and debugging. F. Liu: design methodology, manuscript editing. Q. Wang: research grants, technical guidance, magnet design, system integration, manuscript editing.

Competing interests

The authors declare no competing interests.

Additional information

Correspondence and requests for materials should be addressed to Yaohui Wang or Qiuliang Wang.